applied sciences

MDPI

Article

Flow-Induced Deviation Mechanism and Structural Optimization of Engine Valves Under Braking Conditions

Weitao Si [1], Helin Wang [1], Changhui Zhai [1], Zhongyang Qi [2] and Zhihang Chen [2,*]

[1] State Key Laboratory of Engine and Powertrain System, Weichai Power Co., Ltd., Weifang 261061, China; siweitao@weichai.com (W.S.); wanghelin@weichai.com (H.W.); zhaich@weichai.com (C.Z.)
[2] Aircraft and Propulsion Laboratory, Ningbo Institute of Technology, Beihang University, Ningbo 315800, China; qizhongyang@buaa.edu.cn
* Correspondence: chenzhihang0718@163.com

Abstract

Under braking conditions, the valve is prone to lateral swing, which significantly compromises engine performance and longevity. Research indicates that the asymmetric vortex structures around the valve are one of the primary factors inducing effects such as lateral swing. Therefore, addressing this issue, this paper proposes three structural optimization strategies for controlling the flow around the valve: modifying the valve's camber radius, altering the exhaust port structure that the valve cooperates with, and applying tripwires to the valve. The control effects of these three strategies are demonstrated through three-dimensional numerical simulation techniques, and the control mechanisms are elucidated through vortex field structure analysis. The results reveal that the tripwires improve the asymmetry of the flow field around the valve by disrupting vortex formation at its inception. These analytical results provide specific solutions for reducing the lateral force that induces valve deviation under braking conditions, which possesses important engineering significance.

Keywords: three-dimensional simulation; flow mechanism; structural optimization; engine valve

1. Introduction

The Weichai Exhaust Valve Brake (WEVB) is a passive bleeder-type engine auxiliary brake developed by Weichai Power Co., Ltd. When activated on a downhill coast, an exhaust butterfly valve closes to raise the back pressure in the exhaust manifold, and the resulting pressure pulse unseats the brake exhaust valve near the dead center. A hydraulic latching mechanism inside the rocker arm then locks the brake exhaust valve open by 1–2 mm throughout the compression and power strokes. This sustained leakage gap continuously vents the in-cylinder charge to the exhaust system, dissipating the compression energy and suppressing the gas pressure during the expansion stroke, so that the engine acts as a parasitic energy absorber. However, a recognized limitation is that only one exhaust valve is modulated during braking, in contrast to normal exhaust operation where both valves lift simultaneously. This asymmetric actuation imposes pronounced lateral loading on the brake exhaust valve stem, potentially causing lateral deflection, degraded valve-seat sealing, and uneven wear.

Under braking conditions, the valve has to endure the combined effects of high-speed airflow impact, periodic thermal loads, and mechanical loads, which can easily trigger

Check for updates

Academic Editor: Sébastien Poncet

Received: 27 June 2026
Revised: 3 September 2026
Accepted: 4 September 2026
Published: 8 September 2026

Copyright: © 2026 by the authors. Licensee MDPI, Basel, Switzerland. This article is an open access article distributed under the terms and conditions of the Creative Commons Attribution (CC BY) license.

flow-induced lateral deviation [1–3]. This can lead to abnormal wear between the valve and the valve seat, valve clearance failure, and even valve fracture [4]. This research systematically reveals the analysis of flow-induced deviation mechanisms, deviation suppression techniques, and structural optimization methods, providing theoretical support for improving the dynamic stability of valves under braking conditions.

For the theoretical research, the physical mechanisms of valve flow-induced deviation are deeply revealed through a multidisciplinary approach. Morita et al. [5,6] established a mathematical model of the valve–airflow system based on the coupling theories of structural mechanics, mechanical vibration, and fluid dynamics. They pointed out that the lateral vibration of the valve is mainly caused by the combined action of three mechanisms: vortex-induced vibration (VIV), acoustic resonance, and fluid-elastic instability. Among them, VIV originates from the periodic vortex shedding formed by the airflow around the valve stem. When the vortex shedding frequency approaches the natural frequency of the valve, resonance is triggered. Acoustic resonance is generated by the coupling of pressure waves in the exhaust system and the acoustic modes of the valve structure [7,8]. Fluid-elastic instability is more common in multi-valve parallel arrangements, where dynamic force imbalance between valves is caused by airflow pulsation [9]. Furthermore, the exhaust temperature can reach as high as 500–600 °C. The high-temperature airflow causes a decrease in the elastic modulus of the valve material, reducing the natural frequency of the valve and further exacerbating the risk of VIV [10]. At the same time, the transient airflow impact during valve opening/closing can excite high-frequency vibrations, and the amplitude of these vibrations is positively correlated with the slope of the valve lift curve.

For the deviation suppression and structural optimization techniques, Chan et al. [11] developed a magnetorheological damper. This study employed neural networks to model the magnetorheological damper, demonstrating its potential as a novel semi-active control device in the field of deviation control. Although published relatively early, this research has provided crucial references for subsequent modeling and control strategies of magnetorheological dampers. By adjusting the magnetic field strength in real time to change the damping coefficient, the valve deviation can be reduced. However, this technology requires additional energy input and has high requirements for the precision of the control system. Wilson et al. [12] proposed an asymmetric valve head design. By changing the airflow path, it disrupts the periodicity of vortex shedding, making the VIV frequency deviate from the natural frequency of the valve. Although some progress has been made in the study of deviation, many issues still remain unclear. Although active control technology is effective, it needs to solve problems such as response delay and high energy consumption to meet the requirements of engine transient operating conditions. Lightweight design may reduce the structural stiffness of the valve. It is necessary to achieve a coordinated improvement in light weight and reliability through new materials or novel structures.

This paper investigates the deviation control characteristics during the valve braking process through three-dimensional numerical simulation. Section 2 outlines the test model and the methodologies employed. Section 3 presents and discusses the obtained results. Section 4 offers a discussion on the conclusions drawn from this study.

2. Test Model and Approaches

2.1. Test Model

The computational domain employed in the present study is derived from the Weichai WP13 engine of Weichai Power Co., Ltd., Weifang, Shandong, China and is simplified to capture the flow characteristics relevant to valve deviation during braking operation. Figure 1 shows the model of the valve and its related components. The exhaust port, brake exhaust valve, and cylinder are retained in the geometric model, while the intake port and intake valve are neglected.

The cylinder diameter is 127 mm, the hole diameter on the piston is 83 mm, and the valve head diameter is 40.5 mm. A Cartesian coordinate frame is defined with its origin at the valve center: the y-axis is oriented along the valve stem axis, the x-axis lies in the horizontal direction, and the z-axis completes the right-handed system normal to the xy-plane. The simulation is conducted at the crankshaft angle of 0°, where the pressure differential across the brake exhaust valve attains its maximum value. At this instant, the valve lift is fixed at 1.3132 mm, and the piston is positioned 1.2 mm below the top face of the cylinder. The lower wall of the cylinder is specified as a pressure-inlet boundary, whose total pressure and total temperature are set to 3.866 MPa and 837.9 K, respectively. The end of the exhaust port is defined as a pressure-outlet boundary, with its static pressure set to 0.296 MPa. All walls are set as adiabatic boundaries. Given that fuel delivery is halted under engine braking conditions, combustion is omitted from the simulation. The working fluid is treated as compressible ideal gas. A time step size of 1×10^{-4} s is adopted throughout the transient calculation. The total physical simulation time is 0.1 s, corresponding to 1000 time steps. Twenty iterations are performed per time step, and convergence is judged by residual reductions to 1×10^{-5}.

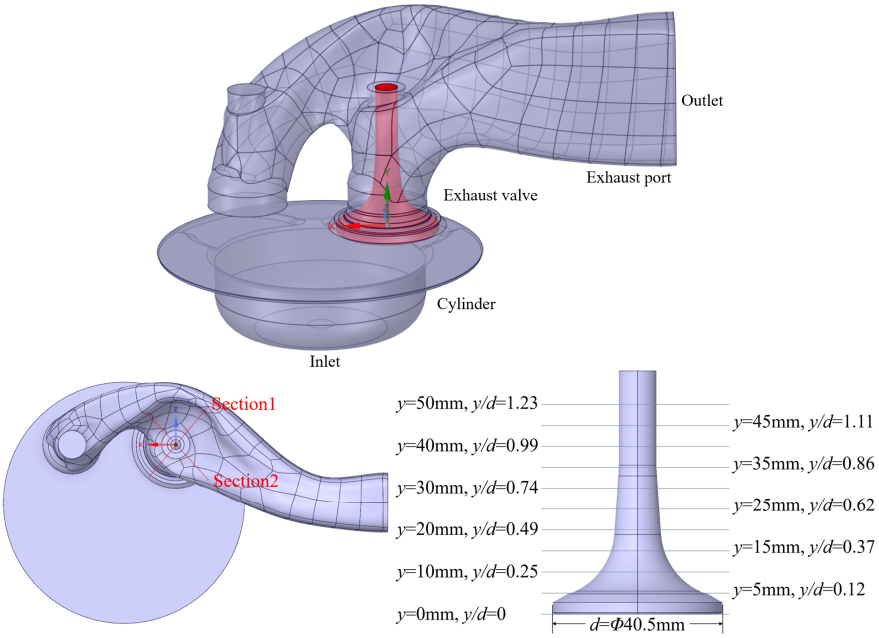


Figure 1. Model of the valve and its related components.

In our previous work [13], the flow-induced deviation mechanism of the engine exhaust valve under braking conditions was investigated, and the present study extends this mechanistic understanding to flow control by proposing and evaluating structural optimization strategies for deviation suppression. Based on previous research, the curved section and cylindrical body of the valve are the main locations where lateral forces are generated, and it is also the key focus of the study on deviation, as shown in Figure 2. Figure 2a illustrates the variation of the cross-sectional force coefficient in the z-direction (C_z) along the valve axis. C_z is defined as:

$$C_z = F_z / \left(0.5 \rho_{\max} V_{\max}^2 d\right)$$

where $\rho_{\max}$ and $V_{\max}$ are the maximum density and velocity of the flow domain, d is the cross-sectional diameter. F_z represents the cross-sectional force in the z-direction, and is defined as:

$$F_z = \int_0^{2\pi} 0.5 p r \sin\theta d\theta$$

where θ is the polar angle distributed circumferentially along the cross-section, r is the cross-sectional radius, and p is the static pressure obtained at the location corresponding to θ. The asymmetric flow shown in Figure 2b develops from the starting vortex at the curved section. Sections 1 and 2 can clearly illustrate the axial development of the flow in the previous research discussions [13]. Therefore, this paper continues to use sections 1 and 2 for further discussion. To investigate the control characteristics of valve deviation, this paper conducts a structural optimization study on the curved section of the valve, presenting three optimization strategies. The first approach involves altering the radius r of the curved segment of the valve, the second entails adjusting the air passage structure, and the third consists of adding tripwires to the curved segment of the valve, as illustrated in Figure 3. For the first approach, r increases from 13 mm to 19 mm in increments of 1 mm. For the second approach, the increase and decrease of flow-channel dimensions were investigated in four directions (inside, outside, left, and right). The detailed research conditions are shown in Table 1. The directions of inside, outside, left, and right follow the coordinate system illustrated in Figure 3b. Combination 1 is the baseline cylindrical geometry. A value of +1 or −1 indicates that the corresponding channel wall is displaced by +1 mm or −1 mm from the baseline geometry. For the third approach, three placement positions of the tripwire (y/d = 0.185, 0.247 and 0.309) along axial directions and two dimensions of tripwires (φ = 0.5 mm and 1 mm) have been selected. The optimal configuration is determined by the peak value and fluctuation of C_z.

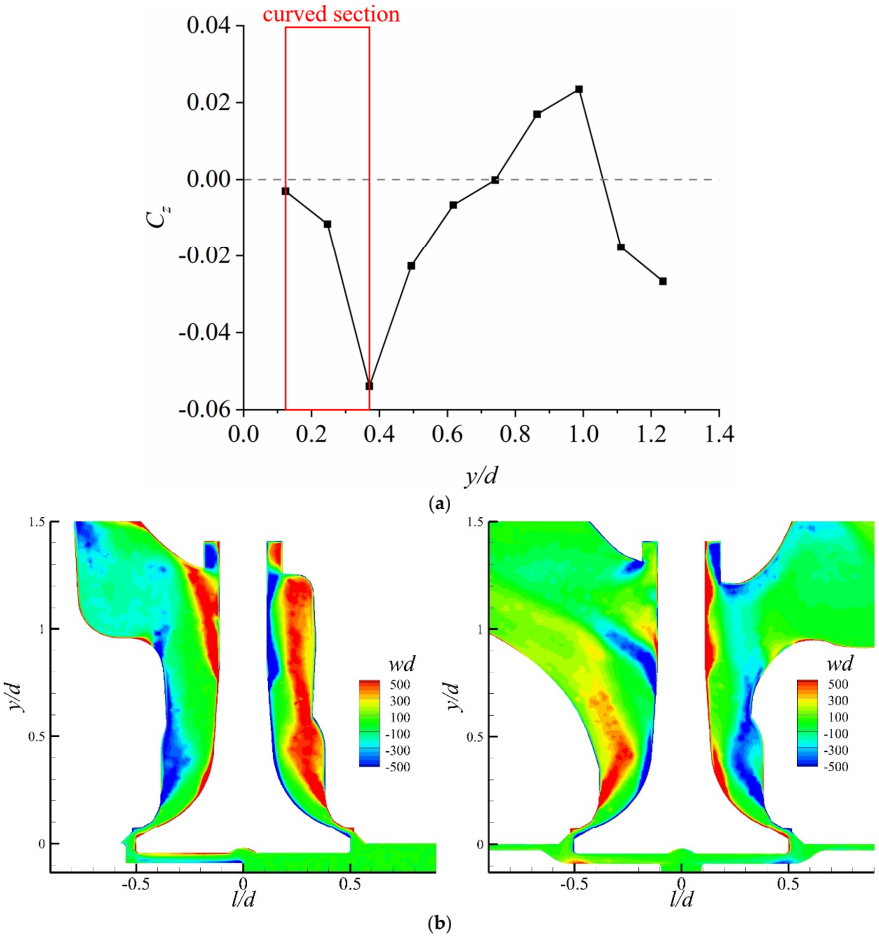


Figure 2. The asymmetric flow characteristics around the valve. (**a**) Variation of sectional lateral force Cz with y/d. (**b**) The contour images of vorticity, section 1, and section 2 shown in Figure 1.

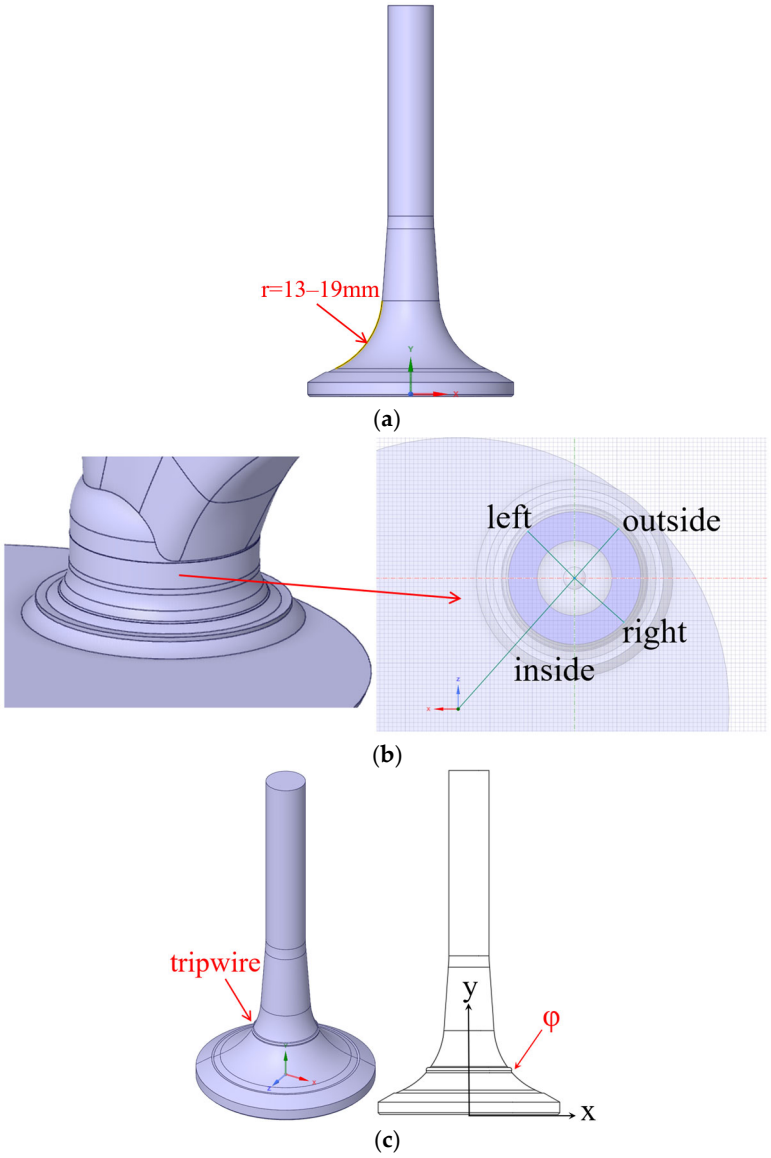


Figure 3. Three optimization strategies. (**a**) Optimization strategy of altering the radius *r* of the curved segment. (**b**) Optimization strategy of adjusting the air passage structure. (**c**) Optimization strategy of adding tripwires to the curved segment.

Table 1. Adjusting the air passage structure (mm).

Combination	Outside	Inside	Left	Right
1	0	0	0	0
2	+1	+1	+1	+1
3	−1	−1	−1	−1
4	+1	−1	0	0
5	−1	+1	0	0
6	0	0	+1	−1
7	0	0	−1	+1
8	+1	+1	−1	−1
9	−1	−1	+1	+1

2.2. Numerical Methods

In this study, ANSYS 2023 Fluent is utilized to conduct a three-dimensional, compressible simulation aimed at analyzing the flow characteristics surrounding the exhaust

valve. Figure 4 illustrates the polyhedral mesh configuration of the model. The mesh size at the valve is 0.2 mm, while the mesh size in the other parts ranges from 0.2 to 1 mm. The height of the first-layer boundary-layer mesh is 0.01 mm, with a growth rate of 1.2. Ten layers of boundary-layer meshes are generated to capture the flow within the boundary layer. Figure 5 illustrates the circumferential pressure coefficient (C_p) distributions under different grid resolutions. The circumferential pressure coefficient, C_p, is defined as:

$$C_p = p / \left(0.5 \rho_{\max} V_{max}^2\right)$$

where p represents the local static gauge pressure evaluated relative to the reference outlet pressure; $\rho_{\max}$ and $V_{\max}$ are the maximum density and velocity of the flow domain. The variations in C_p across the five different grid resolutions are essentially consistent. Therefore, a grid with N = 1.5 million cells is selected as the moderate computational grid for this study, and the minimum orthogonal quality of the grid is 0.2.

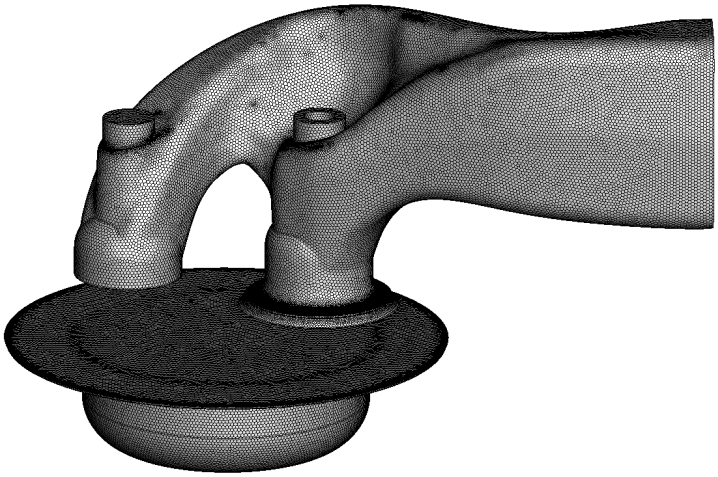


Figure 4. Numerical model and grids.

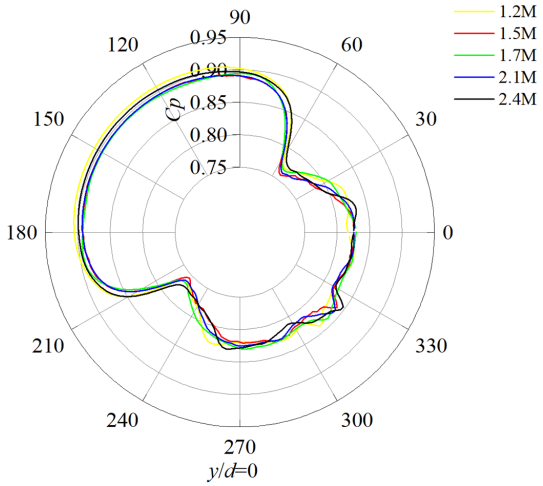


Figure 5. Verification of grid number independence, circumferential pressure (C_p) distributions under different grids.

The transient Reynolds-Averaged Navier–Stokes (RANS) equations are numerically solved through the finite volume method. In terms of spatial discretization for the convective terms in the transport equations, a second-order upwind differencing scheme is applied. Additionally, the coupling between pressure and velocity is addressed using

the Semi-Implicit Method for Pressure-Linked Equations-Consistent (SIMPLEC) approach. This study employs the Shear Stress Transfer (SST) k-ω turbulence model, which has high prediction accuracy for in-cylinder flow [14,15].

3. Results and Discussion

To mitigate the deviation of the valve, this paper implements passive flow control by optimizing the valve structure. This section discusses three distinct control methods, presents their respective control effects, and elucidates the underlying control mechanisms.

3.1. Optimization Strategy of Altering the Radius r of the Curved Segment

Figure 6 illustrates a comparison about the development curves of the sectional lateral force along the axial direction for different r (shown in Figure 3a). As can be seen from the figure, when r = 13 mm, near the valve tail end where y/d = 1.23, $C_z = -0.058$. The sectional lateral forces at the head and tail ends of the valve are opposite in direction, resulting in a significant bending moment. Additionally, in the section of the valve where $0 < y/d \leq 0.4$, C_z experiences a rapid decline and a change in direction, which may accelerate the induction of oscillation [16–18]. As r increases, the rate of decline of C_z in the interval $0 < y/d \leq 0.4$ slows down, the valley near y/d = 0.4 flattens out, and its value decreases, which is conducive to reducing valve oscillation. In the interval $0.4 < y/d \leq 1.1$, the sectional lateral force coefficient C_z fluctuates around zero and changes direction twice, reducing the magnitude of the lateral force. At the valve tail end, as r increases, the value of C_z decreases, resulting in a smaller overall lateral force for the valve. In particular, when r = 18 mm, there is a noticeable control effect.

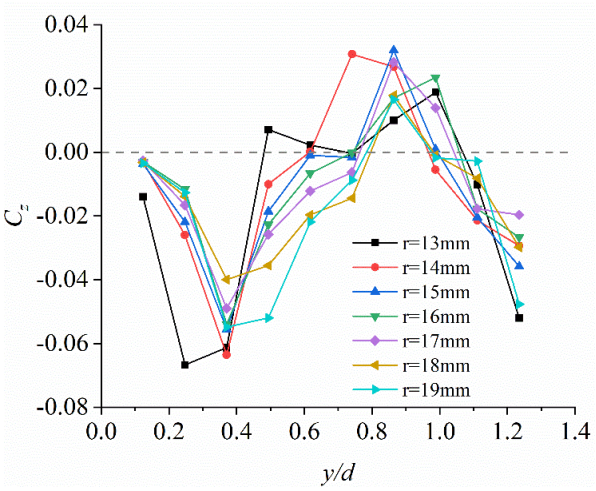


Figure 6. Variation of sectional lateral force Cz with y/d at different r.

Figure 7 presents the vorticity contour for sections 1 and 2 at radii of 13 mm, 15 mm, 18 mm, and 19 mm. From Figure 7a–d, it can be observed that, within the range of y/d = 0.7–1.3, the vortex on the right side of the valve adheres to the valve surface, generating greater suction, while the vortex on the left side has lifted off from the wall, resulting in reduced suction on the wall. Due to the differential circumferential forces acting on the valve, the lateral force on the section increases at y/d = 1.23. In Figure 7e–h, it can be seen that the vortex adhering to the valve surface on the right side has lifted off, weakening the suction on the surface, while the left-side vortex remains in a lifted state [19–21]. This leads to a reduction in the asymmetry of the circumferential pressure distribution on the section, consequently decreasing the lateral force on the section at y/d = 1.23.

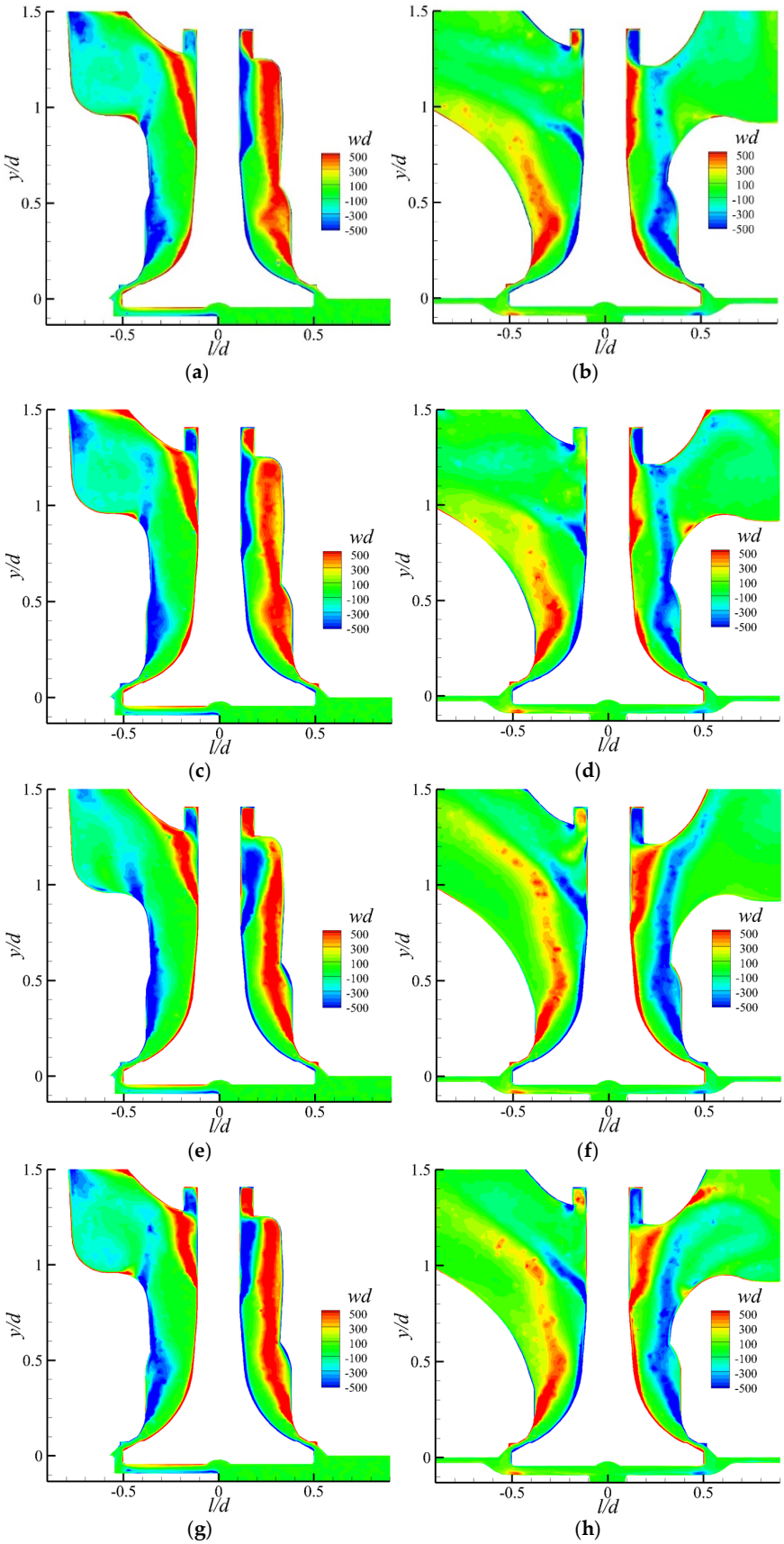


Figure 7. The contour images of vorticity of optimization strategy 1. (**a**) section 1, r = 13 mm. (**b**) section 2, r = 13 mm. (**c**) section 1, r = 15 mm. (**d**) section 2, r = 15 mm. (**e**) section 1, r = 18 mm. (**f**) section 2, r = 18 mm. (**g**) section 1, r = 19 mm. (**h**) section 2, r = 19 mm.

3.2. Optimization Strategy of Adjusting the Air Passage Structure

Figure 8 illustrates a comparison about the development curves of the sectional lateral force along the axial direction for different air passage structures (shown in Figure 3b and Table 1) at r = 16 mm. Adjusting the dimensions of the exhaust port in various directions is intended to change the intensity of vortex formation, which subsequently affects the valve surface pressure at corresponding circumferential locations [22,23]. From Figure 8, it can be observed that near the section at y/d = 0.12, the starting position of the vortex, there is a noticeable impact on the lateral force of the section. As the vortex develops axially, the influence of the flow on the valve surface converges and becomes disordered [24,25]. Moreover, the maximum sectional lateral force is reduced from 0.09 to 0.04 at y/d =0.037, indicating that modifying the exhaust passage has a positive effect on mitigating valve lateral swing [26].

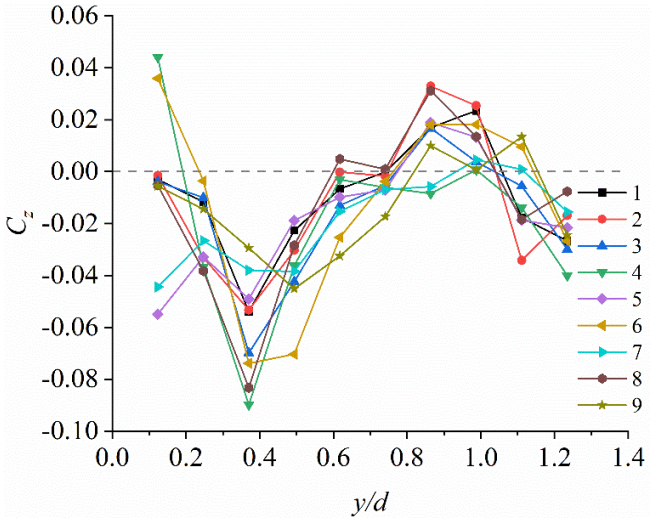


Figure 8. Variation of sectional lateral force *Cz* with y/d at different air passage structures at r =16 mm.

Figure 9 presents the vorticity contour for sections 1 and 2 at combinations 2, 4, and 7. The primary reason for selecting combinations 2, 4, and 7 is that their lateral forces at section y/d = 0.12 are approximately zero, greater than zero, and less than zero, respectively. It can be observed that different initiation conditions lead to significant differences in the overall flow field structure, but the control effects are not clear. Compared with the structural optimization of the valve, the optimization scheme for the exhaust passage involves excessive modifications and is not conducive to engineering applications [27–30].

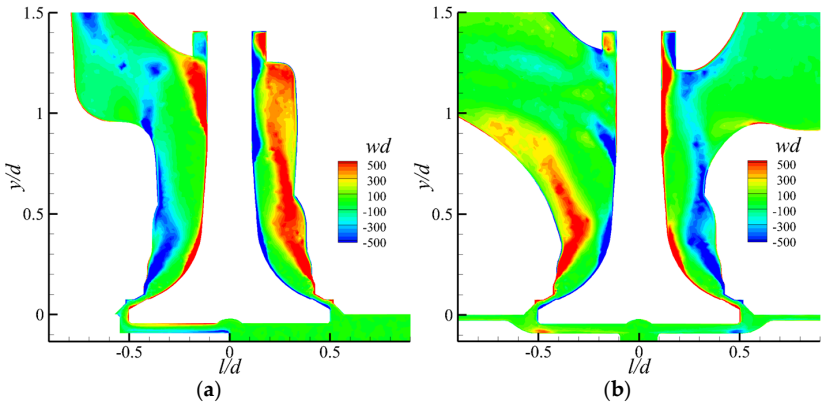


Figure 9. *Cont.*

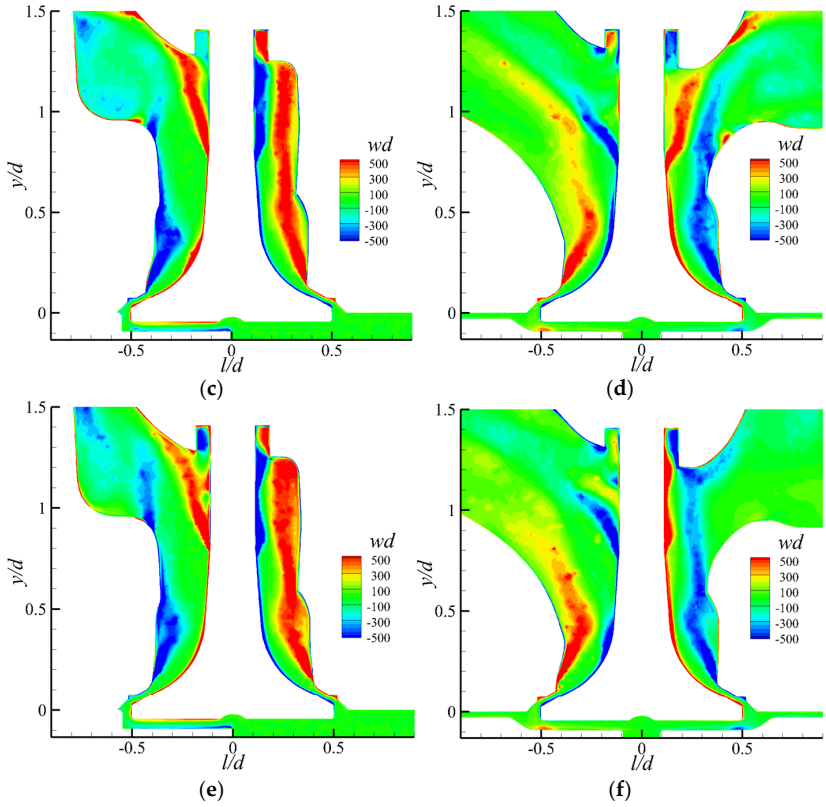


Figure 9. The contour images of vorticity of optimization strategy 2. (**a**) section 1 at combination 2. (**b**) section 2 at combination 2. (**c**) section 1 at combination 4. (**d**) section 2 at combination 4. (**e**) section 1 at combination 7. (**f**) section 2 at combination 7.

3.3. Optimization Strategy of Adding Tripwires to the Curved Segment

Figure 10 illustrates a comparison about the development curves of the sectional lateral force along the axial direction for different tripwire positions (shown in Figure 3c). It can be seen that the higher the installation position (the larger y/d) of the tripwire, the greater the negative peak of C_z, indicating more severe deterioration of the sectional lateral force [31,32]. In particular, when the tripwire is added at $y/d = 0.309$, the lateral force is the most unfavorable with the peak value exceeding that of the original valve. In contrast, adding the tripwire at $y/d = 0.185$ yields the most prominent suppression effect on the lateral force peak. In the range $0 < y/d < 0.4$, the rapid drop of C_z is effectively inhibited and the fluctuation of C_z is substantially reduced. When the tripwire is added at $y/d = 0.247$, the fluctuation amplitude of C_z in the range $0.6 < y/d < 1.1$ is the smallest among all tested schemes, resulting in a more uniform and stable lateral force distribution.

The corresponding vorticity contours are presented in Figure 11. The installation position has a significant impact on the flow field symmetry. As shown in Figure 11b ($y/d = 0.185$), the vortex structures on both the left and right sides of the valve are generally symmetrical, with uniform wall attachment and the minimum circumferential pressure difference. The symmetry of the vortices on both sides slightly decreases in Figure 11d ($y/d = 0.247$), resulting in a secondary control effect [33,34]. The vortex structure on the right side of the valve re-attaches to the wall, leading to a destruction of flow field symmetry and a weakened lateral force suppression effect in Figure 11f ($y/d = 0.309$). The results indicate that installing the tripwire too high tends to induce local vortex reattachment, and $y/d = 0.185$ is the optimal axial installation position. According to the result analysis, the asymmetric vortex occurs at the curved section of the valve. The smaller the y/d of the tripwire's placement position on the curved section, the more conducive it is to the generation of the symmetric vortex, and the stronger the control effect will be.

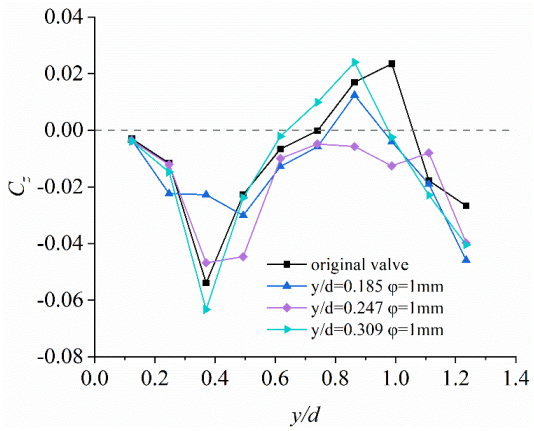


Figure 10. Variation of sectional lateral force *Cz* with y/d at different tripwires.

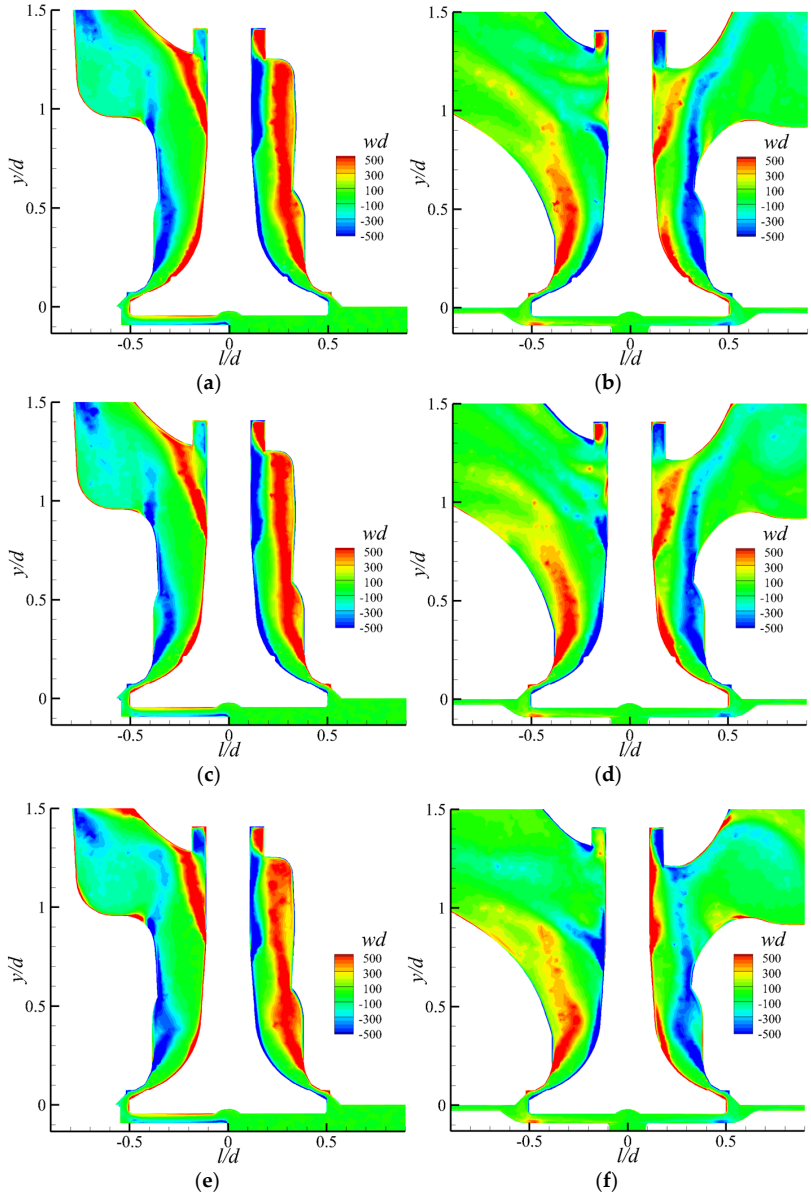


Figure 11. The contour images of vorticity of optimization strategy 3. (**a**) section 1, y/d = 0.185, φ = 1 mm. (**b**) section 2, y/d = 0.185, φ = 1 mm. (**c**) section 1, y/d = 0.247, φ = 1 mm. (**d**) section 2, y/d = 0.247, φ = 1 mm. (**e**) section 1, y/d = 0.309, φ = 1 mm. (**f**) section 2, y/d = 0.309, φ = 1 mm.

Figure 12 illustrates a comparison about the development curves of the sectional lateral force along the axial direction for different tripwire diameters φ (shown in Figure 3c). Both diameters can effectively smooth the C_z curve and reduce lateral force fluctuation. The 1 mm tripwire has stronger inhibition on the C_z peak and a more significant stabilization effect, indicating that appropriately increasing the tripwire diameter is conducive to improving the lateral force control effect.

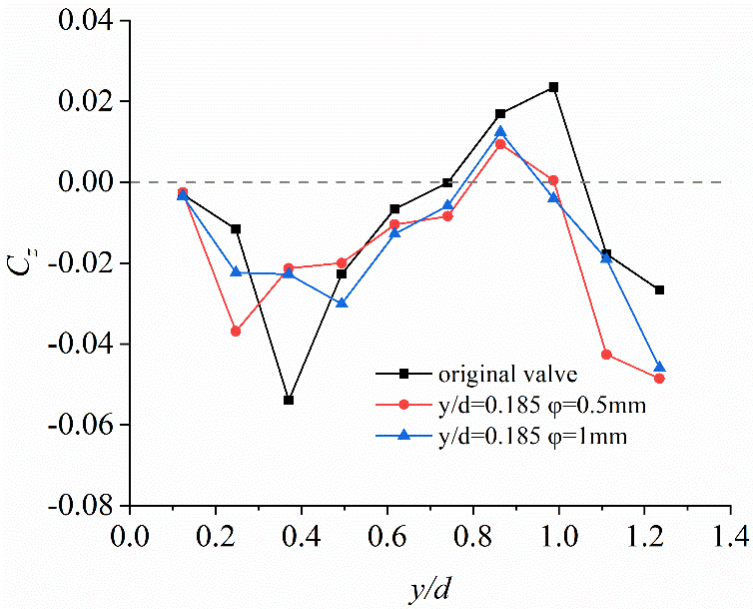


Figure 12. Variation of sectional lateral force *Cz* with φ at y/d = 0.185.

Figure 13 shows the vorticity of tripwires with different diameters. At the same installation position (y/d = 0.185), the vortex on the right side of the valve in Figure 13b (φ = 0.5 mm) showed obvious wall attachment, resulting in an increase in the asymmetry of the flow field and an increase in the circumferential pressure difference. Figure 13d (φ = 1 mm) has stronger disturbance on the boundary layer, which can effectively inhibit the re-attachment of one side vortex. The vortex structure on both sides is more symmetrical, which is more conducive to reducing the section lateral force and yaw moment. The research results indicate that the larger the diameter of the tripwire, the stronger the interference it causes to the surface flow at the curved section of the valve. This affects the surface flow separation, weakens the intensity of the generated vortices, leading to an enhanced control effect in vortex generation.

3.4. Effects of Additional Crankshaft Angle Within Braking Conditions

To examine whether the control effect persists at neighboring crankshaft angles within the braking condition, two additional conditions are simulated at crankshaft angles of 690° and 30°, which are 30° before and after the reference condition at 0°. The boundary conditions of these cases are summarized in Table 2, and all other numerical settings are identical to those described in Section 2. At these two additional angles, the original valve and the optimal tripwire configuration (y/d = 0.185, φ = 1 mm) are compared in Figures 14 and 15. It can be observed that the optimized valve effectively reduces the peak and fluctuation of *Cz*, indicating that the identified control mechanism is not limited to a single instantaneous flow state within the braking condition.

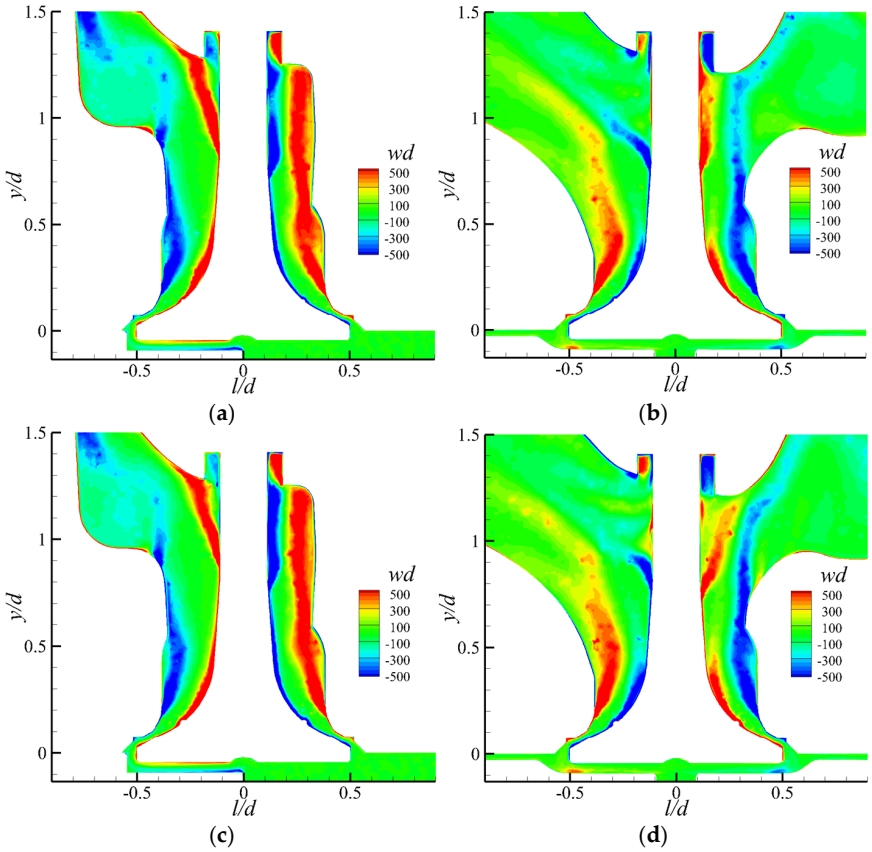


Figure 13. The contour images of vorticity of optimization strategy 3. (**a**) section 1, y/d = 0.185, φ = 0.5 mm. (**b**) section 2, y/d = 0.185, φ = 0.5 mm. (**c**) section 1, y/d = 0.185, φ = 1 mm. (**d**) section 2, y/d = 0.185, φ = 1 mm.

Table 2. Boundary conditions of crankshaft angles of 690° and 30°.

Crankshaft Angle	Valve Lift	Piston Stroke	Inlet Pressure	Inlet Temperature	Outlet Pressure
690°	0.6764 mm	17.5132 mm	2.263 MPa	735.1 K	0.215 MPa
30°	1.0783 mm	15.6156 mm	0.947 MPa	570 K	0.298 MPa

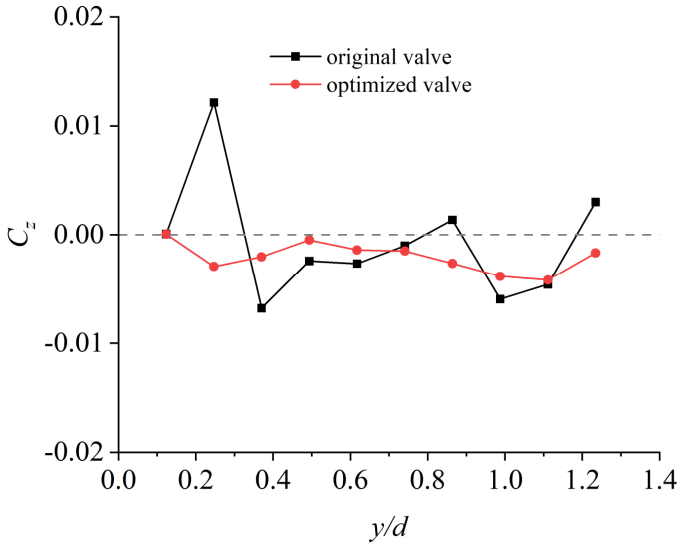


Figure 14. Variation of sectional lateral force *Cz* at crankshaft angles of 690°.

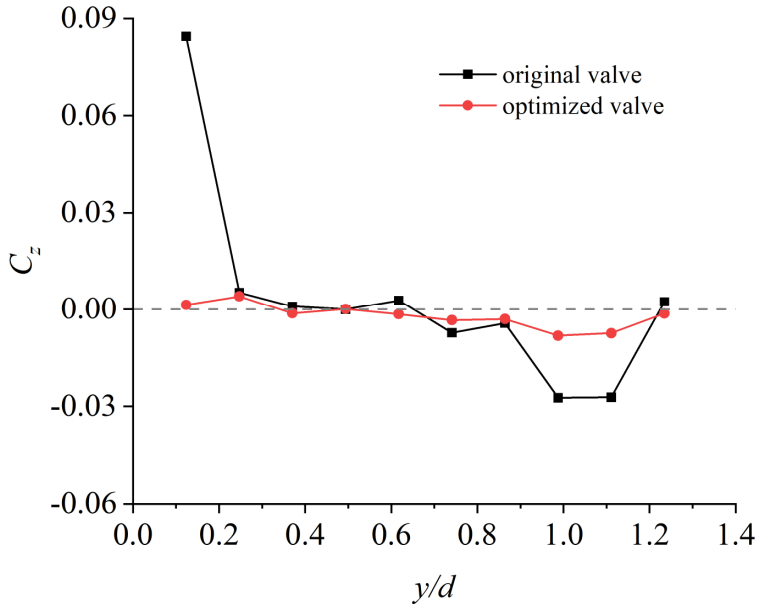


Figure 15. Variation of sectional lateral force *Cz* at crankshaft angles of 30°.

4. Conclusions

Three-dimensional compressible numerical simulations are carried out to reveal the flow-induced deviation mechanism of engine exhaust valves under braking conditions.

Through three-dimensional compressible numerical simulations, we investigate the control characteristics of valve deviation under braking conditions and determine the control effectiveness. Results show that asymmetric vortex structures around the valve are the primary trigger of deviation. The asymmetric multi-vortex flow along the valve axis evolves the lateral force and yaw moment. Three structural optimization strategies are analyzed. Increasing the radius of the valve curved section can slow down the variation of the lateral force coefficient and reduce the yaw moment with the optimal effect at r = 18 mm. Adjusting the exhaust port structure can suppress vortex initiation and reduce the peak lateral force, but the modification range is large so the engineering applicability is poor. Adding tripwires on the curved section can break the initial asymmetric vortex and improve flow field symmetry. The optimal scheme is to install a tripwire with φ = 1 mm at y/d = 0.185, which presents the most stable and remarkable lateral force suppression effect. This study provides effective passive control methods and theoretical support for reducing valve lateral force under braking conditions. In addition, further research can be carried out to simulate the force and displacement of the valve by adopting the fluid–structure interaction method, so as to verify whether the optimization methods can reduce valve wear.

Author Contributions: Validation, W.S.; investigation, H.W.; writing—original draft preparation, C.Z.; writing—review and editing, Z.Q.; supervision, Z.C. All authors have read and agreed to the published version of the manuscript.

Funding: The study is supported by the Research Fund of State Key Laboratory of Engine and Powertrain System (skleps-sq-2024-095).

Institutional Review Board Statement: Not applicable.

Informed Consent Statement: Not applicable.

Data Availability Statement: The raw data supporting the conclusions of this article will be made available by the authors on request.

Conflicts of Interest: The State Key Laboratory of Engine and Powertrain System is affiliated with Weichai Power Co., Ltd. Authors Weitao Si, Helin Wang, and Changhui Zhai are members of this laboratory and are also employed by Weichai Power Co., Ltd. The engine used in this study was provided by the laboratory. The study is supported by the Research Fund of State Key Laboratory of Engine and Powertrain System (skleps-sq-2024-095). We disclose these relationships and confirm that they did not influence the content or conclusions of this work.

References

1. Wang, S. The Application of Diesel Engine: From 21st Century to Modern Life. *Highlights Sci. Eng. Technol.* **2024**, *114*, 37–42. [CrossRef]
2. Junhong, Z.; Jun, H. CAE process to simulate and optimise engine noise and vibration. *Mech. Syst. Signal Process.* **2006**, *20*, 1400–1409. [CrossRef]
3. Ungar, E.E.; Ross, D. Vibrations and noise due to piston-slap in reciprocating machinery. *J. Sound Vib.* **1965**, *2*, 132–146. [CrossRef]
4. Deulgaonkar, V.R.; Ingolikar, N.; Borkar, A.; Ghute, S.; Awate, N. Failure analysis of diesel engine piston in transport utility vehicles. *Eng. Fail. Anal.* **2021**, *120*, 105008. [CrossRef]
5. Morita, R.; Inada, F.; Mori, M.; Tezuka, K.; Tsujimoto, Y. CFD Simulations and Experiments of Flow Fluctuations Around a Steam Control Valve. *J. Fluids Eng.* **2006**, *129*, 48–54. [CrossRef]
6. Yonezawa, K.; Ogawa, R.; Ogi, K.; Takino, T.; Tsujimoto, Y.; Endo, T.; Tezuka, K.; Morita, R.; Inada, F. Flow-induced vibration of a steam control valve. *J. Fluids Struct.* **2012**, *35*, 76–88. [CrossRef]
7. Wang, B.; Wang, Y.; Liang, W.; Sheng, S.; Guo, J.; Zhang, L. Numerical simulation on the sound field of gas valve due to inner leakage. In *Proceedings of the ASME Pressure Vessels and Piping Conference*; ASME: New York, NY, USA, 2009; Volume 43642, pp. 467–471.
8. Ng, K.W. Control valve noise. *Isa Trans.* **1994**, *33*, 275–286. [CrossRef]
9. Morita, R.; Inada, F.; Mori, M.; Tezuka, K.; Tsujimoto, Y. Flow induced vibration of a steam control valve in middle-opening condition. In *Proceedings of the ASME Pressure Vessels and Piping Conference*; ASME: New York, NY, USA, 2005; Volume 41898, pp. 485–490.
10. Sun, Y.; Zhang, Y.; Chen, Z.; Lin, X.; Zhao, X.; Li, Y.; Yao, S.; Wang, X.; Zheng, X. Investigation on compression-springback performance of the SUS301 stainless steel gasket considering the residual stress. *Mater. Today Commun.* **2022**, *33*, 104296. [CrossRef]
11. Chang, C.C.; Roschke, P. Neural network modeling of a magnetorheological damper. *J. Intell. Mater. Syst. Struct.* **1998**, *9*, 755–764. [CrossRef]
12. Wilson, N.D.; Watkins, A.J.; Dopson, C. Asymmetric valve strategies and their effect on combustion. In Proceedings of the International Congress and Exposition, Detroit, MI, USA, 1–5 March 1993.
13. Mo, W.; Dou, Z.; Sun, Q.; Chen, Z. Flow Mechanism Analysis of Engine Valve Deviation Under Braking Conditions. *Fluids* **2026**, *11*, 87. [CrossRef]
14. Gao, F.D.; Wang, D.X.; Wang, H.D.; Jia, M.M. Numerical analysis and verification of the gas jet from aircraft engines impacting a jet blast deflector. *Chin. J. Mech. Eng.* **2018**, *31*, 86. [CrossRef]
15. Debnath, A.; Roy, B.; Sinha, A. Assessment of RNG k-ε, SST k-ω and Reynolds stress models for numerical simulation of DLR scramjet engine. *Int. J. Mech. Prod. Eng. Res. Dev.* **2019**, *9*, 1157–1166. [CrossRef]
16. Jia, M.; Xie, M.; Wang, T.; Peng, Z. The effect of injection timing and intake valve close timing on performance and emissions of diesel PCCI engine with a full engine cycle CFD simulation. *Appl. Energy* **2011**, *88*, 2967–2975. [CrossRef]
17. Demir, U.; Coskun, G.; Soyhan, H.S.; Turkcan, A.; Alptekin, E.; Canakci, M. Effects of variable valve timing on the air flow parameters in an electromechanical valve mechanism—A cfd study. *Fuel* **2022**, *308*, 121956. [CrossRef]
18. Vimalananth, V.T.; Nedunchezhiyan, M.; Ramalingam, S.; Natesan, P.; Sampath, S. Hybrid computational fluid dynamics (CFD)–experimental characterization of swirl-enhancing intake valve designs for improved combustion and reduced emissions. *Appl. Therm. Eng.* **2025**, *289*, 129640. [CrossRef]
19. Reitz, R.D.; Rutland, C.J. Development and testing of diesel engine CFD models. *Prog. Energy Combust. Sci.* **1995**, *21*, 173–196. [CrossRef]
20. Clenci, A.C.; Iorga-Simăn, V.; Deligant, M.; Podevin, P.; Descombes, G.; Niculescu, R. A CFD (computational fluid dynamics) study on the effects of operating an engine with low intake valve lift at idle corresponding speed. *Energy* **2014**, *71*, 202–217. [CrossRef]
21. Peng, Z.; Jia, M. Full engine cycle CFD investigation of effects of variable intake valve closing on diesel PCCI combustion and emissions. *Energy Fuels* **2009**, *23*, 5855–5864. [CrossRef]
22. Martos, F.J.; Soriano, J.A.; Braic, A.; Fernández-Yáñez, P.; Armas, O. A cfd modelling approach for the operation analysis of an exhaust backpressure valve used in a euro 6 diesel engine. *Energies* **2023**, *16*, 4112. [CrossRef]

23. Motwani, R.; Gandolfo, J.; Gainey, B.; Filipi, Z.; Lawler, B. A 3D CFD-FEA co-simulation study of low thermal effusivity TBCs applied to the piston and valves of an SI engine. *Int. J. Engine Res.* **2024**, *25*, 2142–2162. [CrossRef]
24. Ahsan, M.; Noman, M. Improving Internal Combustion Engine Performance through Inlet Valve Geometry and Spray Angle Optimization: Computational Fluid Dynamics Study. *Eng. Proc.* **2024**, *72*, 6. [CrossRef]
25. Liu, J.; Yang, R.; Liu, Z.; Liu, J. A CFD-assisted investigation into the mechanism behind the surge in NO_2 emissions from methanol/diesel dual fuel engines. *J. Clean. Prod.* **2025**, *489*, 144750. [CrossRef]
26. Żyłka, M.; Marszałek, N.; Żyłka, W. Numerical simulation of pneumatic throttle check valve using computational fluid dynamics (CFD). *Sci. Rep.* **2023**, *13*, 2475. [CrossRef]
27. Pham, V.C.; Le, V.V.; Choi, J.H.; Lee, W.J. CFD Analysis of Equivalence Ratio Effects on Combustion and Emissions in a Methanol–Diesel Dual-Fuel Marine Engine. *Energies* **2026**, *19*, 626. [CrossRef]
28. Griaznov, V.; Trigui, N.; Affes, H.; Smith, D. CFD based shape optimization of IC engine. *Oil Gas Sci. Technol.* **1999**, *54*, 297–307. [CrossRef]
29. Menaa, A.; Lounici, M.S.; Amrouche, F.; Loubar, K.; Kessal, M. CFD analysis of hydrogen injection pressure and valve profile law effects on backfire and pre-ignition phenomena in hydrogen-diesel dual fuel engine. *Int. J. Hydrogen Energy* **2019**, *44*, 9408–9422. [CrossRef]
30. Bari, S.; Saad, I. CFD modelling of the effect of guide vane swirl and tumble device to generate better in-cylinder air flow in a CI engine fuelled by biodiesel. *Comput. Fluids* **2013**, *84*, 262–269. [CrossRef]
31. Wu, Y.; Wang, Y.; Zhen, X.; Guan, S.; Wang, J. Three-dimensional CFD (computational fluid dynamics) analysis of scavenging process in a two-stroke free-piston engine. *Energy* **2014**, *68*, 167–173. [CrossRef]
32. Qian, J.; Wei, L.; Jin, Z.; Wang, J.-K.; Zhang, H.; Lu, A.-L. CFD analysis on the dynamic flow characteristics of the pilot-control globe valve. *Energy Convers. Manag.* **2014**, *87*, 220–226. [CrossRef]
33. Mattarelli, E.; Rinaldini, C.A.; Cantore, G. CFD optimization of a 2-stroke range extender engine. *Int. J. Automot. Technol.* **2015**, *16*, 351–369. [CrossRef]
34. Harshavardhan, B.; Mallikarjuna, J.M. Effect of piston shape on in-cylinder flows and air–fuel interaction in a direct injection spark ignition engine—A CFD analysis. *Energy* **2015**, *81*, 361–372. [CrossRef]

Disclaimer/Publisher's Note: The statements, opinions and data contained in all publications are solely those of the individual author(s) and contributor(s) and not of MDPI and/or the editor(s). MDPI and/or the editor(s) disclaim responsibility for any injury to people or property resulting from any ideas, methods, instructions or products referred to in the content.